International Journal of Engineering Trends and Technology
ISSN: 2231-5381/ https://doi.org/10.14445/22315381/IJETT-V74I5P131

Volume 74 Issue 5, 495-513, May 2026
© 2026 Seventh Sense Research Group®

Original Article

Digital Twin Supported AI-Assisted Synchronization and Intelligent FRT for Grid-Connected Photovoltaic Inverters

Sanju[1], Kusum Lata Agarwal[2], Satya Sai Srikant[3], S Nallusamy[4]

[1]*Department of Electrical and Electronics Engineering, SRM Institute of Science and Technology, Delhi-NCR Campus, Modinagar, Ghaziabad, Uttar Pradesh, India.*
[2]*Professor and Dean of Academics, Karnavati University, Gandhinagar, Gujarat, India.*
[3]*Department of Electronics and Communication Engineering, SRM Institute of Science and Technology, Delhi-NCR Campus, Modinagar, Ghaziabad, Uttar Pradesh, India.*
[4]*School of Engineering Management and Continuing Education, Jadavpur University, Kolkata, India.*

[2]*Corresponding Author : kusum@karnavatiuniversity.edu*

Received: 09 February 2026 Revised: 16 March 2026 Accepted: 21 April 2026 Published: 30 May 2026

Abstract - *The presence of high PV in low-voltage microgrids creates operating difficulties like voltage sag, harmonics, and frequency variation. Such issues may disturb inverter operation and enhance current stress and DC-link voltage stress. The integrated method presented in this paper includes a calibrated digital twin, enhanced synchronization, and an intelligent fault ride-through strategy in a single practical workflow. A physics-informed model that consists of the dynamics of the PV array, DC-link, converter, and the grid system constructs the digital twin. The lab data used for its calibration ensures that its output matches real disturbances for controller tuning. In addition, via learning of the residual phase and frequency errors encountered during distorted voltage sags, an A2I-Phase Locked Loop (PLL) successfully enhances the performance of a regular Synchronous Reference Frame (SRF)-PLL. Ultimately, an intelligent layer of FRT decreases the active current safely and injects the reactive current for voltage support and decides tripping, which is done using clear limits on current and DC link voltage. Experimental validation, conducted on a programmable PV and grid emulation platform, demonstrates that the digital twin accurately reproduces the measured DC-link voltage and current waveforms. Furthermore, the AI-PLL exhibits superior angle tracking performance under distorted conditions, and the FRT strategy effectively reduces peak current and DC-link stress while maintaining reactive power support during deep voltage sags.*

Keywords - *AI-assisted PLL, Digital twin, Fault ride-through, Grid synchronization, Photovoltaic inverter, Reactive current injection, Voltage sag.*

1. Introduction

The structure of contemporary power distribution technologies is undergoing considerable changes because of renewable technologies. Solar photovoltaic technologies, in particular, have attracted a great deal of attention for their modular design and scalability as well as declining installation costs. Government policies are also a major force. Plus, global initiatives directed at sustainable energy are speedily deploying PV systems in low-voltage distribution networks and microgrids. Although there are advantages to PV systems, their growing penetration will also create several operational problems that may impact grid stability and power quality.

Low-voltage distribution networks are high impedance non-linear loading conditions and low inertia systems, which are therefore much more prone to disturbances, including voltage sags, harmonics, and frequency variations. With non-ideal conditions, maintaining stable operation with grid-connected PV inverters becomes a challenge. More specifically, when disturbances occur in the grid, phase and frequency estimation degrade, control accuracy is put at risk, and pressure on critical components like the DC-link is increased, affecting the overall reliability.

Grid regulations require PV inverters nowadays to be equipped with functionality of FRT. It means the inverter should keep connected to the grid. This is during disturbance for a longer duration, with reactive current injection and keeping a safe current level. Standards such as IEEE 1547-2018 formalize such requirements with the expectation of voltage and frequency ride-through and reactive power support [1]. Nevertheless, effective FRT operation is very challenging because of the interconnections of synchronization, current control, and protection. Degradation in synchronization performance may pass through the control system, compromising the ride-through capability.

Several researchers have investigated PV System monitoring, fault-detection, synchronization, and ride-through control (maybe ‘sag ride-through control’). In the early studies, researchers mainly focused on component fault detection of photovoltaic arrays. Most works identify faults such as mismatch losses, ground faults, and string failure. These works were mainly based on modeling and signal processing methods. With the improvement of sensing and data acquisition technologies, more recent methods integrating statistical methods and machine learning techniques have appeared for real-time fault diagnosis. Although these methods enhance detection performance, their impact is confined to monitoring only and does not affect action control.

To mitigate grid distortion impacts, many improved synchronization techniques based on PLL have been proposed. Methods such as SRF-PLL, SOGI-based structures, and adaptive filtering techniques have displayed enhanced robustness to harmonic distortion and voltage unbalance. Most of these techniques, however, rely on a fixed control structure and are not adaptable to varying system dynamics and parameter uncertainties.

Due to the advancements in Digital Twin (DT) techniques, it is quite possible to achieve real-time representation, prediction, and optimization of the system in modern power systems. On the other hand, AI-based control methods have attracted improvements in adaptability and robustness during grid variation. Most of the existing approaches handle monitoring, synchronization, and FRT separately. Moreover, the integration of DT-based control and AI-assisted coordinated inverter operation is not as much.

As a result, a unified framework integrating the digital twin modelling with AI-assisted synchronization and intelligent FRT control is warranted for the reliable operation of grid-connected PV systems under non-ideal grid conditions.

Integration of renewable energy at speed is transforming the power distribution system. In particular, continuous cost reduction and scalability of Solar PV technology are gaining popularity, as stated in previous studies. In addition, governmental actions and clean energy goals further boost this [2, 3]. However, when the penetration of PV systems in low-voltage feeders is very high, a number of operational issues arise [4]. These feeders generally have high impedance and non-linear loads, which further increase voltage sag, increase harmonic distortion, and cause larger frequency variations.

PV inverters must stay connected to the grid during an abnormal operation and provide support to the grid through the injection of reactive current within permissible current limits. Achieving these conditions is not easy due to disturbance in the grid, which leads to desynchronization, decreased current margin, and more stress on the DC-link.

Despite the wide-ranging investigation of fault detection in PV systems, most approaches treat the fault diagnosis and the inverter ride-through as independent one. Nonetheless, a calibrated digital twin unites both these problems on a common platform. A digital twin confirms the capacity to simulate disturbances that occur in the grid, estimate uncertain parameters, and improve monitoring and control capabilities in real-time operating conditions [8-10]. Table 1 gives a quick overview of major research areas and their focus.

Table 1. Short summary of related PV fault and monitoring studies

Topic	Main focus	Refs.
Diagnostic modeling	Mismatch effects and diagnostic models for PV systems	[5]
Thermography inspection	Field and plant-level thermal inspection for fault identification	[6]
Data-driven diagnosis	Real-time monitoring, statistical methods, and ML/ANN-based fault classification	[7]
Digital twin support	Disturbance replication, parameter estimation, and control support	[8]
Smart PV and net zero design	Model-based design support for smart PV and net-zero systems	[9, 10]

1.1. Research Gap and Problem Introduction

Even with all these, there remain some crucial gaps. Most of the studies, in particular, consider fault detection, synchronization, and FRT as separate problems, despite their strong interdependence in reality. Moreover, traditional synchronization strategies are incapable of learning and do not perform well in significantly distorted and uncertain grid environments. Many FRT strategies rely on ideal phase estimation and accurate system models, making them unsuitable for practical implementation. Ultimately, there has not been an adequate investigation into the combined application of digital twin technology with Artificial Intelligence (AI) in coordinated control of synchronization and ride-through.

A lot of the PV fault analysis research literature focuses on array-side fault detection, while the inverter synchronization and current control loops are often modeled as ideal. Numerous FRT strategies depend on perfect phase locking and an accurate model of the plant. However, these models are not generally applicable to low-voltage microgrids. The performance of the PLL circuit for phase estimation may be affected by distortion, inaccuracies in plant parameters may limit control performance, and a compromise on DC-link voltage control and reactive current supply to faults may be needed. For non-ideal grid environments, a practical and comprehensive solution is needed for digital twin calibration/synchronization and safe FRT operation.

1.2. Contributions and Novelty of the Work

To address these limitations, a digital twin-supported, AI-assisted framework for synchronization and intelligent FRT in grid-connected PV inverters is presented. The proposed approach consists of a single architecture to achieve real-time system modelling and learning-based synchronization.

A digital twin is calibrated to accurately mimic the behavior of the PV inverter system, enabling continuous monitoring and tuning of the parameters. An AI-assisted phase-locked loop is introduced to enhance phase and frequency tracking during grid disturbances. Also, an FRT control layer is designed to manage current limiting, reactive power support, and protection decisions based on real-time operating conditions.

The proposed framework is different from the existing methods because it combines digital twin modelling with AI-driven control in a closed-loop, which allows for adaptive and predictive operation at non-ideal grid conditions. The effectiveness of the proposed method is validated through experimental analysis.

It provides enhanced synchronization performance and improved FRT capability over conventional methods. The contributions of this present work and a comparison with the existing studies are given in Table 2.

2. Literature Survey

Recent studies have improved PV fault monitoring and diagnosis, but most works still treat monitoring and ride-through control as separate problems. This section gives a short review of the main methods and shows the gap addressed in this work.

2.1. PV Faults and Monitoring Techniques

Many studies report PV fault diagnosis using model-based methods, signal processing, and thermal inspection. Reviews summarize common PV faults and monitoring system designs. Real-time and plant-level fault detection methods are also available, including methods linked with MPPT behavior [11]. Infrared thermography is widely used for fault inspection in both lab and field conditions [12]. Reflectometry and failure experiments also help identify string-level faults [13]. Ground-fault detection remains an important safety topic, and several robust methods have been reported.

2.2. Data-Driven Diagnosis and Fault Tolerance

Data-driven methods support PV fault diagnosis when fault patterns are complex. Kernel-based models and feature optimization are used for PV fault diagnosis [14]. Statistical monitoring and detection methods are discussed [15, 16]. Fault-tolerant and reconfiguration methods are also studied to maintain power generation under faulty conditions. Other works use inferential monitoring, outlier detection, Kalman filtering, and reliability analysis to improve diagnosis and decision support [17].

2.3. The Need for Digital Twin-Supported Control

The literature shows strong progress in monitoring and fault diagnosis, but inverter ride-through still depends on fast control action and accurate synchronization during faults. Some studies connect diagnosis with energy assessment and power management [11], but a complete link between monitoring, synchronization, and ride-through control is still limited.

A calibrated digital twin can fill this gap by linking plant signals, synchronization, and ride-through control in one workflow. Table 3 summarizes the related literature.

Table 2. Main contributions of this work

No.	Contribution
C1	A calibrated digital twin of a grid-connected PV inverter test setup is established using a comprehensive PV–DC-link–converter–grid model, with parameters refined through laboratory-based tuning.
C2	A learning-assisted PLL (AI-PLL) is presented to improve SRF-PLL phase and frequency tracking during voltage sag and harmonic distortion.
C3	An intelligent FRT layer is developed to handle current limiting, reactive support, and trip decisions based on sag level, DC-link stress, and protection limits.
C4	Experimental results confirm twin-to-plant matching and show improved synchronization and ride-through response under grid disturbances.

Table 3. Literature survey of PV monitoring and diagnosis

Ref.	Year	Scope and main technique	Data-driven element	Key strengths and limitations
[14]	2009	PV mismatch loss analysis and behaviour	Model based	Not designed for fast converter events
[17]	2016	Electrical fault study for PV arrays; fault signatures	Limited	Not a control-oriented ride-through solution
[2]	2018	Review of PV fault detection and monitoring systems	Review	Implementation details vary by plant
[3]	2016	PV system control and design foundations	Limited	Not focused on disturbance ride-through
[4]	2019	Review of protection challenges and PV fault diagnosis	Review	Lacks DT-based coordination with control
[18]	2019	Robust synchronization under unbalance and distortion using SOGI/IFLL-type methods	No	Improves angle tracking but is not linked to calibrated digital twin tuning
[19]	2021	Low-voltage ride-through improvement using fast sequence handling control	Limited	Mainly microgrid-focused and not unified with PV inverter digital twin calibration.
[20]	2022	Review of FRT methods and control approaches in PV power plants	Review	Does not provide an integrated digital twin and synchronization approach
[21]	2023	Review of power quality improvement during PV fault ride through	Review	Strong overview, but no experimental digital twin-based disturbance replay
[22]	2023	Review of digital twin technology in solar PV generation	DT review	Digital twin survey and not converter control grade validation for ride through
[22]	2024	Systematic review of digital twins for PV systems	DT review	Review level does not show end-to-end tuning with ride-through constraints.
[23]	2025	Systematic review of digital twin for solar PV with applications and prospects.	DT review	Review paper and no unified AI- assisted synchronization with constrained ride-through.
Proposed work–		DT with AI- assisted PLL and Intelligent fault ride-through for microgrids.	DT and AI	Joint modelling, synchronization, and ride through under explicit safety constraints.

2.4. Critical Comparison with Recent Literature

Table 4 highlights the recent activities; nevertheless, it has been inferred that earlier research works are inadequate and scattered in dealing with grid-connected PV inverter operation.

Most studies that utilize Digital Twin (DT) technology for their analyses emphasize monitoring, forecasting, and system. Although these methods provide useful insights into how the system responds and acts, they do not participate in real-time inverter control and Fault Ride-Through (FRT) decision-making. In the same vein, AI-based approaches are mostly used for fault detection and classification, rather than for synchronization or control loops.

Utilizing improved Phase-Locked Loop (PLL) techniques, advanced synchronization techniques are highly capable of matching the phase of distorted voltage patterns. Nevertheless, such approaches are usually elaborated without plant-specific dynamic structures and parameter uncertainty compliant controls. In addition, they are not utilizing system feedback in real-time from a digital twin for tuning or correction. Most FRT strategies put forward in the literature are mainly based on current injection and limiting. In practical low-voltage microgrids, the assumption of ideal synchronization and accurate system models is not true. Consequently, their performance worsens in the presence of large disturbances and uncertain conditions. In contrast, the proposed work introduces a unified framework that tightly integrates digital twin modeling, AI- assisted synchronization, and intelligent FRT control within a closed-loop architecture. The digital twin is not only used for monitoring but also for disturbance replay, parameter calibration, and controller validation.

The proposed AI- assisted PLL learns residual synchronization errors and dynamically compensates for them under distorted conditions. Furthermore, the intelligent FRT layer coordinates current limiting, reactive support, and protection decisions based on real-time system states. Therefore, unlike existing approaches that address these challenges in isolation, the proposed method provides a coordinated and adaptive solution that enhances inverter stability and reliability under non-ideal grid conditions. Therefore, unlike existing approaches that address these challenges in isolation, the proposed method provides a coordinated and adaptive solution that enhances inverter stability and reliability under non-ideal grid conditions.

Table 4. Critical comparison of recent literature with the proposed work

Category	Main Approach	DT Integration	AI Integration	Key Limitations
DT-based PV systems (2024-2026)	Monitoring, forecasting, parameter estimation	Used for simulation and diagnostics	Limited to prediction tasks	No real-time control integration; not used for synchronization or FRT
AI-based fault detection (2023-2025)	ML/DL-based classification and protection	Not used	Used for fault detection	No role in inverter control, synchronization, or ride-through
Enhanced PLL techniques (2023-2025)	SOGI, SRF-PLL, adaptive filtering	Not used	Minimal learning capability	Fixed structure; poor adaptability under severe distortion
FRT control strategies (2022-2024)	Reactive power injection, current limiting	Not used	Minimal or no AI	Assume ideal synchronization and accurate models
DT + AI frameworks (2025-2026)	System-level optimization and smart grids	High-level integration	AI for prediction/ optimization	Lack o f inverter-level validation and closed-loop control
Proposed Work	DT-assisted synchronization+ intelligent FRT	Real-time calibrated DT integrated in the control loop	AI-assisted PLL + intelligent decision layer	Unified closed-loop framework addressing synchronization, FRT, and parameter uncertainty

3. System Modelling and Digital-Twin Development

3.1. PV Array and DC-Link Model

A single-diode equivalent circuit is employed to model the PV array. The output current of the PV array is expressed as

$$I_{pv} = I_{ph} - I_o\left(exp\left(\frac{V_{pv}+I_{pv}R_S}{nN_SV_T}\right)-1\right)-\left(\frac{V_{pv}+I_{pv}R_S}{R_{sh}}\right) \quad (1)$$

where I_{pv} denotes the array output current (A), I_{ph} represents the photocurrent (A), and I_o is the diode reverse saturation current (A). The terminal voltage of the PV array is given by V_{pv} (in V), while R_s and R_{sh} correspond to the series and shunt resistances (in Ω), respectively. The parameter n is the diode ideality factor, N_s is the number of series-connected cells, and V_T Is the thermal voltage defined as $V_T = \frac{k_BT}{q}$, where k_B is Boltzmann’s constant (J/K), T is the cell temperature (K), and q is the electron charge (C). The photocurrent is influenced by both irradiance and temperature and can be expressed as

$$I_{ph} = \left(I_{sc„ref} + \alpha_{Isc}(T - T_{ref})\right)\frac{G}{G_{ref}} \quad (2)$$

where G represents the solar irradiance (W/m^2), $I_{sc,ref}$ is the reference short-circuit current (A), α_{Isc} denotes the temperature coefficient (A/K), T_{ref} is the reference temperature (K), and G_{ref} is the reference irradiance (W/m^2).

The temperature dependence of the diode saturation current is described by,

$$I_o(T) = I_{o,ref}\left(\frac{T}{T_{ref}}\right)^3 exp\left(\frac{qE_g}{nk_B}\left(\frac{1}{T_{ref}}-\frac{1}{T}\right)\right) \quad (3)$$

where $I_{o,ref}$ denotes the reference saturation current (A), and E_g is the semiconductor bandgap energy.

The dynamics of the DC-link capacitor are governed by,

$$C_{dc}\frac{dV_{dc}}{dt} = I_{pv} - I_{inc,dc} \quad (4)$$

where C_{dc} is the DC-link capacitance (F), V_{dc} is the DC-link voltage (V), and $I_{inc,dc}$ represents the DC current drawn by the inverter (A). Assuming negligible conversion losses, the instantaneous power balance between the DC and AC sides can be approximated as:

$$V_{dc}I_{inc,dc} \approx p_{ac} \quad (5)$$

where p_{ac} is the instantaneous active power delivered to the AC side. In the synchronous dq reference frame, the instantaneous active and reactive powers are given by:

$$p_{ac} = \frac{3}{2}(v_di_d + v_qi_q), \qquad q_{ac} = \frac{3}{2}(v_di_q - v_qi_d) \quad (6)$$

where v_d and v_q denote the dq-axis voltage components (V), and i_d and i_q are the corresponding current components (A). The reactive power q_{ac} It is considered positive when injected into the grid.

By substituting (5) and (6) into (4), the DC-link voltage dynamics can be rewritten as

$$C_{dc}\frac{dV_{dc}}{dt} = I_{pv} - \frac{3}{2}\left(\frac{v_d i_d + v_q i_q}{V_{dc}}\right) \qquad (7)$$

Equation (7) highlights the DC-link overvoltage mechanism under deep voltage sags: when the exported active power collapses while current limiting constraints are in place. i_d, the DC-link energy can accumulate and raise V_{dc}.

3.2. Reference-Frame Transformations and Grid Emulator

For three-wire, balanced operation (zero-sequence neglected), the Clarke transformation is

$$\begin{bmatrix} v_\propto \\ v_\beta \end{bmatrix} = \frac{2}{3}\begin{bmatrix} 0 & -\frac{1}{2} & -\frac{1}{2} \\ 0 & \frac{\sqrt{3}}{2} & -\frac{\sqrt{3}}{2} \end{bmatrix}\begin{bmatrix} v_a \\ v_b \\ v_c \end{bmatrix} \qquad (8)$$

and the Park transformation is,

$$\begin{bmatrix} v_d \\ v_q \end{bmatrix} = \begin{bmatrix} \cos\theta & \sin\theta \\ -\sin\theta & \cos\theta \end{bmatrix}\begin{bmatrix} v_\propto \\ v_\beta \end{bmatrix} \qquad (9)$$

where v_a, v_b, and v_c are the three-phase voltages, $v_\propto$ and v_β are the stationary αβ-frame voltages, v_d and v_q are the synchronous dq-frame voltages, and θ denotes the rotating frame electrical angle.

The programmable grid emulator is described in the true grid-voltage-aligned synchronous frame (with $\theta = \theta_g$), such that $v_{gq}(t) = 0$ and,

$$v_g^{dq}(t) = \begin{bmatrix} v_{gd}(t) \\ v_{gq}(t) \end{bmatrix} = V_g(t)\begin{bmatrix} 1 \\ 0 \end{bmatrix} \qquad (10)$$

where $v_g^{dq}(t)$ is the grid-voltage vector in the synchronous frame, $v_{gd}(t)$ and $v_{gq}(t)$ are its d- and q-axis components, and $V_g(t)$ denotes the grid-voltage magnitude (specified consistently as peak or rms, and as phase-neutral or line-line according to the experimental setup). A voltage sag is imposed through

$$V_g(t) = \begin{Bmatrix} V_{nom,} & t < t_f. & \\ k_{sag}V_{nom,} & t_f \le t \le t_f + T_{sag}, & 0 < k_{sag} \le 1 \\ V_{nom,} & t > t_f + T_{sag}, & \end{Bmatrix} \qquad (11)$$

where V_{nom} is the nominal grid-voltage magnitude, t_f is the sag inception time, T_{sag} is the sag duration, and $k_{sag}$is the sag depth factor. A frequency excursion is represented by

$$f(t) = \begin{Bmatrix} f_{nom,} & t < t_\omega. & \\ f_{nom} + \Delta f. & t_\omega \le t \le t_\omega + T_\omega, & \omega\,(t) = 2\Pi f t \\ f_{nom,} & t > t_\omega + T_\omega, & \end{Bmatrix} \qquad (12)$$

where $f(t)$ is the grid frequency, f_{nom} is the nominal grid frequency, Δf is the frequency step magnitude, t_ω is the start time of the frequency event, T_ω is its duration, and $\omega\,(t)$ is the grid angular frequency. The corresponding grid electrical angle is $\theta_g\,(t) = \theta_g\,(0) + \int_0^t \omega\,(\tau)d\tau$, where $\theta_g\,(0)$ is the initial grid angle, and τ is the integration variable

3.3. Digital Twin Architecture and Calibration Workflow

Figure 1 depicts the digital twin architecture employed in this study. The twin comprises a physics-based core that reproduces the fast electrical dynamics of the PV source, DC-link, and inverter-side response, together with a measurement interface that acquires time-synchronized laboratory signals for parameter identification.

The twin is used in two complementary modes: (i) forward simulation to replay disturbances and evaluate control actions under repeatable operating conditions, and (ii) inverse calibration to estimate model parameters that are not directly measurable from the experimental setup.

The selection of the experimental operating region is guided by PV array characteristics under Standard Test Conditions (STC), as illustrated in Figure 2. The corresponding I–V and P–V characteristics are used to establish repeatable operating points, ensuring that the calibration spans the full voltage–current domain of interest.

Sampling is performed around the maximum power point and its surrounding regions to guarantee model validity under both MPPT and curtailed operating conditions.

The calibration and validation arrangement is illustrated in Figure 3. A programmable PV source is used to impose repeatable operating points, while a grid emulator applies voltage sag and frequency profiles according to (11) and (12).

The measurement locations shown in Figure 3 are used consistently throughout the paper. DC-link sensing supports validation of the DC-link dynamics in (7), PCC voltage sensing provides the input to the PLL defined in (14)-(15), and current sensing is used to enforce the inverter current constraint in (23). Calibration is formulated as a weighted trajectory matching problem that estimates the parameter vector ϕ (R_s, R_{sh}, filter parameters, and sensor gains) by minimizing the mismatch between measured and simulated trajectories:

$$\phi^* = \arg min \sum_{k=1}^{N}\left(\omega_v\left\|V_{dc}[k] - \widehat{V_{dc}}[k;\phi]\right\|_2^2 + \omega_i\|i^{dq}[k] - \hat{\imath}^{dq}[k;\phi\|_2^2\right) \qquad (13)$$

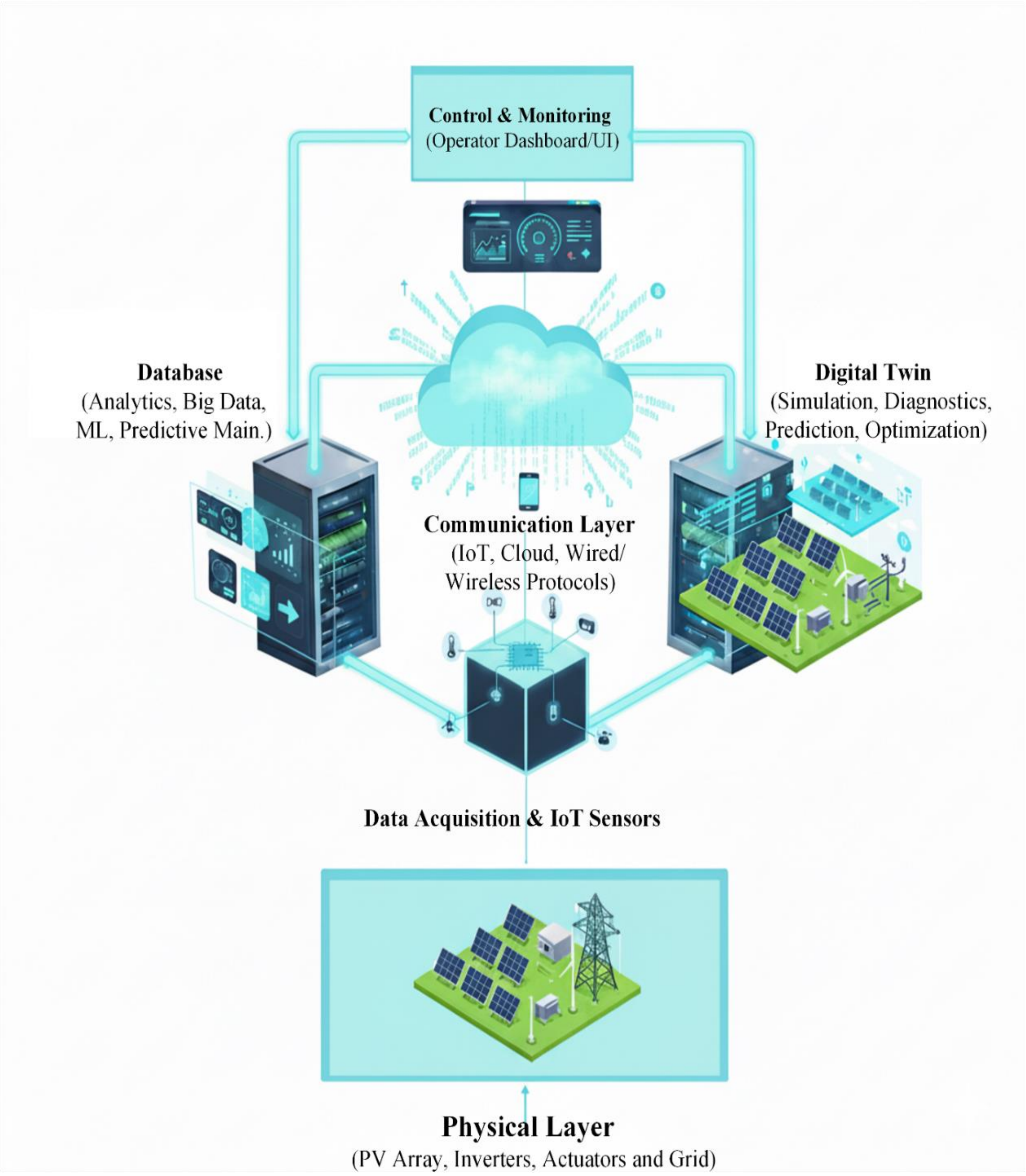

Fig. 1 Digital twin architecture for grid-connected PV inverter operation

where $\widehat{(.)}$ denotes the digital-twin prediction and ω_v, ω_i are weighting factors. The identified parameter set ϕ^* is then fixed for the subsequent test campaign, and the calibrated twin is used for disturbance replay and for generating model-consistent internal variables required by the control and protection studies.

3.4. Assumptions and Fidelity of the Digital Twin

The accuracy of the proposed framework is strongly influenced by the fidelity of the Digital Twin (DT) model and its capability to emulate the real-time dynamics of the physical system. The following assumptions are therefore made:

- Model Structure: The DT is based on a physics-informed model of the PV array, DC-link, and inverter dynamics. Fast electromagnetic transients beyond the control bandwidth are neglected, which is consistent with standard converter control design.
- Parameter Calibration: Model parameters are identified using trajectory matching (13), ensuring that the DT reproduces measured DC-link voltage and current responses under disturbances. This reduces model mismatch and improves reliability.
- Measurement Availability: It is assumed that PCC voltage, inverter currents, and DC-link voltage are

measurable with sufficient accuracy and sampling rate, which is practical in modern inverter platforms.

- Real-Time Execution: The DT operates at a slower supervisory timescale compared to the inner control loop. Therefore, strict real-time execution at switching frequency is not required.

The experimental validation results in Section 5.2 demonstrate that the DT accurately captures system dynamics under voltage sag and swell conditions, thereby justifying its use for control support and disturbance replay.

4. Proposed Learning-Assisted Synchronization and Intelligent FRT

4.1. Control Overview

Figure 3 outlines the proposed control framework. The inner current loop regulates inverter currents in the synchronous frame to accurately track the reference components. (i_d^*, i_q^*). The reference signals are generated by outer loops responsible for DC-link voltage regulation and reactive current injection during grid disturbances. The synchronization unit provides the phase angle estimate $\hat{\theta}$ used in the Park transformation (9).

The proposed learning-assisted PLL augments the baseline SRF-PLL during sags and waveform distortion. In addition, a supervisory FRT layer generates fault-conditioned current references and executes trip arbitration when protection limits are exceeded.

The calibrated digital twin is used to replay disturbances under repeatable conditions and to generate labelled trajectories for model validation and learning-stage development.

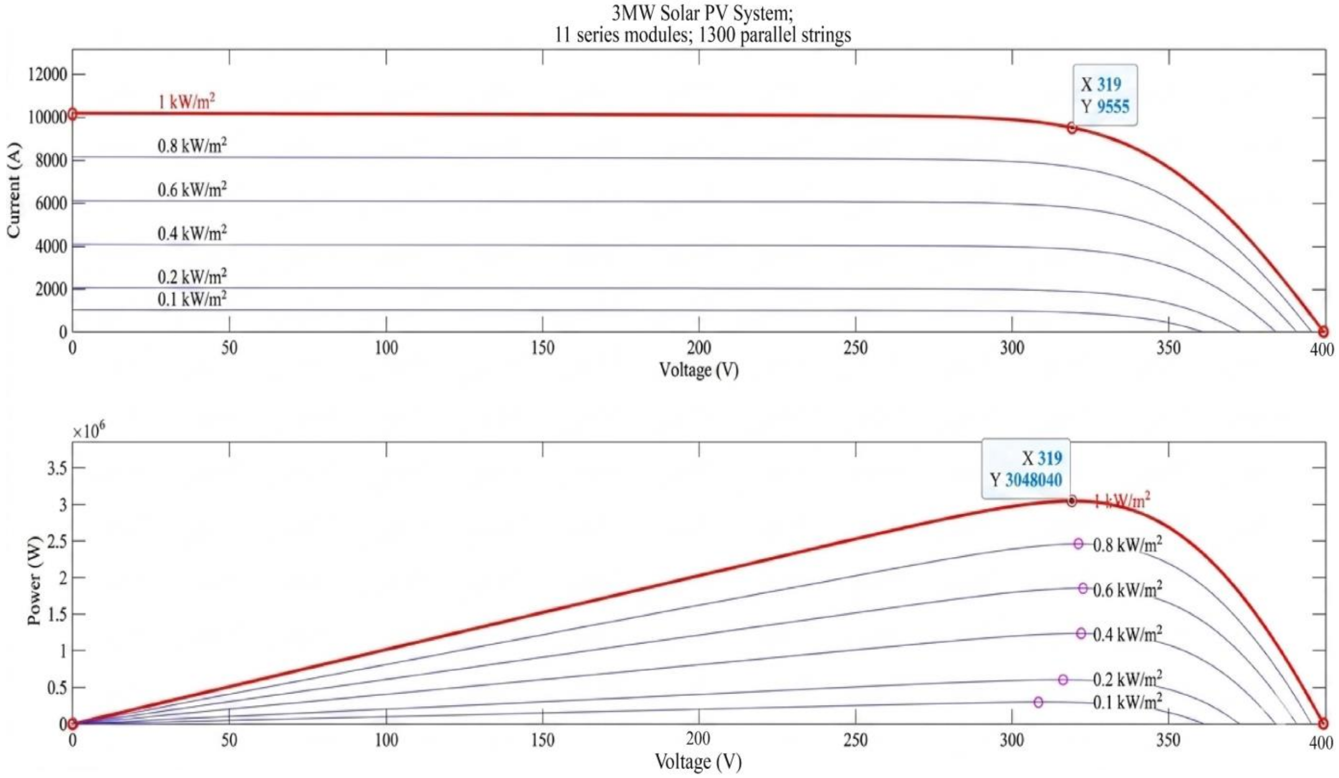

Fig. 2 PV array characteristics under standard test conditions (STC)

4.2. Real-Time Implementation Considerations

The proposed framework is designed with practical, real-time implementation constraints in mind. The inner current control loop operates at high frequency (kHz range), while the digital twin and AI-assisted modules operate at a supervisory level with lower update rates.

The AI-assisted PLL augmentation introduces only a feedforward correction term, which requires minimal computational overhead compared to conventional PLL structures. The neural network used in (16) is lightweight and can be implemented on embedded processors or DSP platforms. Furthermore, the digital twin is not required to run at the switching frequency.

Instead, it operates in parallel for disturbance replay, parameter estimation, and supervisory control tuning. This separation of timescales ensures that the proposed approach is computationally feasible for real-time deployment.

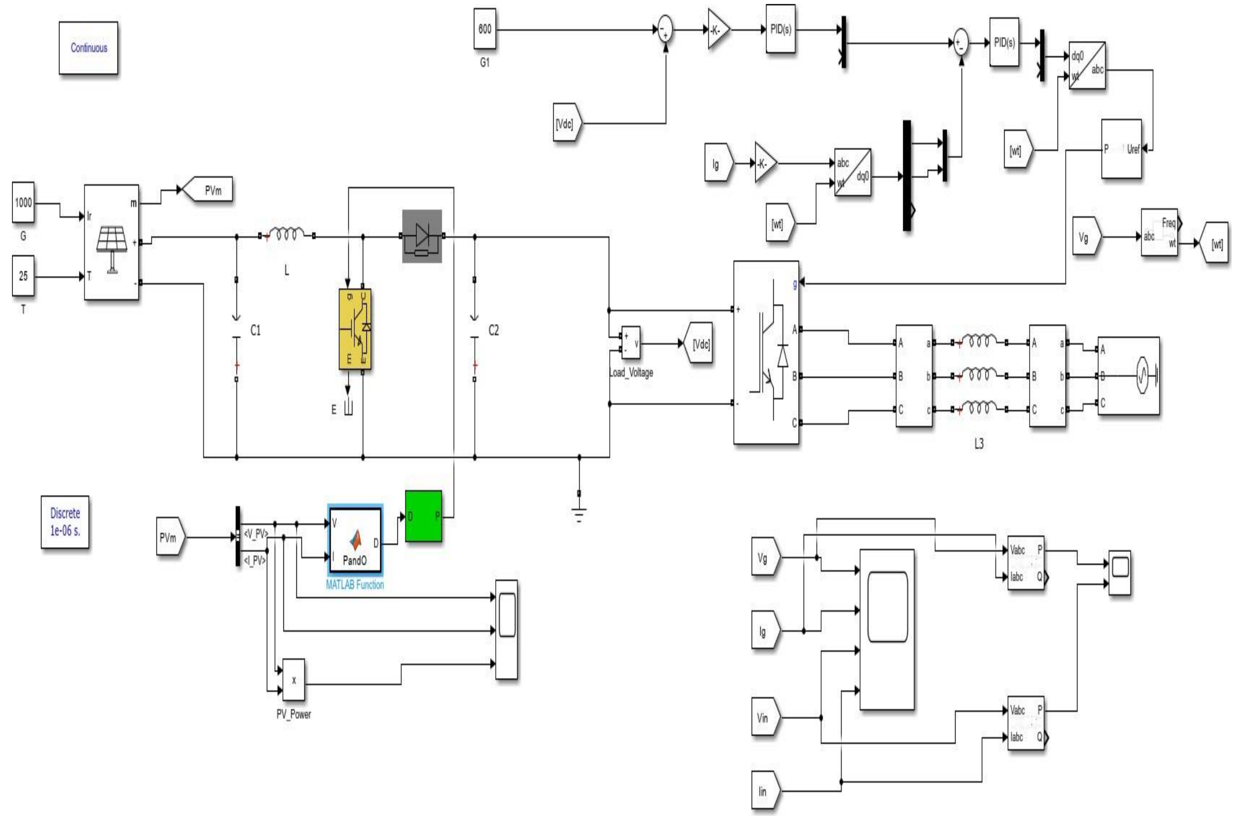

Fig. 3 Simulink setup for grid-connected system

4.3. Baseline SRF-PLL and Learning-Assisted Augmentation

A SRF-PLL employs the q-axis component of the point of common coupling (PCC) voltage as the phase-error signal, given by

$$e_\theta(t) = v_q(t) \tag{14}$$

where $e_\theta(t)$ denotes the phase-error signal, $v_q(t)$ represents the q-axis PCC voltage component in the synchronous dq frame, and t is time. The quantity $v_q(t)$ is obtained through the Park transformation using the estimated phase angle $\hat{\theta}(t)$, which corresponds to the grid angle estimated by the PLL.

The conventional PLL dynamics are described as

$$\frac{d\hat{\theta}}{dt} = \widehat{\omega}, \widehat{\omega}(t) = \omega_{nom} + K_p e_\theta(t) + K_i \int_0^t e_\theta(\tau)\, d\tau \tag{15}$$

where $\widehat{\omega}(t)$ is the estimated grid angular frequency, ω_{nom} is the nominal grid angular frequency, and K_p and K_i denote the proportional and integral gains of the PLL controller, respectively. The variable τ represents the integration variable. To enhance synchronization performance under distorted grid conditions, the PLL is augmented with a data-driven correction term applied to the frequency estimate:

$$\widehat{\omega}_{aug}(t) = \widehat{\omega}(t) + \Delta\widehat{\omega}_{aug}(t), \quad \Delta\widehat{\omega}_{aug}(t) = N_\psi(z(t)) \tag{16}$$

where $\widehat{\omega}_{aug}(t)$ is the corrected frequency estimate, $\Delta\widehat{\omega}_{aug}(t)$ represents the learned correction term, and $N_\psi(.)$ denotes a feedforward neural network parameterized by ψ. The input feature vector $z(t)$ consists of measured and/or digital twin-consistent variables, including the d- and q-axis voltage components. $v_d(t)$ and $v_q(t)$, the derivative $\dot{v_q}(t)$, the baseline frequency estimate $\widehat{\omega}(t)$, and the grid voltage magnitude $V_g(t)$. The augmented phase angle $\hat{\theta}_{aug}(t)$ is obtained by integrating the augmented frequency, i.e. $\frac{d\,\hat{\theta}_{aug}(t)}{dt} = \widehat{\omega}_{aug}$, where $\hat{\theta}_{aug}(t)$ represents the improved estimate of the grid angle. The neural network is trained using disturbance replay data, where a reference angle $\theta[k]$ is provided by the grid emulator or an equivalent high-accuracy measurement system. The training objective minimizes the phase tracking error while penalizing excessive correction magnitude:

$$\mathcal{L}_{PLL}(\psi) = \frac{1}{N}\sum_{k=1}^{N}\left(\theta[k] - \hat{\theta}_{aug}[k]\right)^2 + \lambda\left(\Delta\widehat{\omega}_{aug}[k]\right)^2 \tag{17}$$

where $\mathcal{L}_{PLL}(\psi)$ denotes the loss function, ψ represents the neural network parameters, N is the number of training samples, and k is the discrete-time index. The term $\lambda > 0$ is a regularization coefficient that limits excessive correction, ensuring stable and smooth frequency estimation.

4.4. Dataset Generation and Training Procedure

The dataset used for training the AI-assisted PLL is generated using a combination of digital twin simulations and experimental measurements obtained from the grid emulator setup.

4.4.1. Dataset Composition

- Voltage sag scenarios: 10% to 60% depth
- Harmonic distortion levels: 2% to 10% THD
- Frequency deviations: ±2 Hz around nominal frequency
- Duration: multiple disturbance windows of varying lengths

Each dataset sample consists of:

$$z(t) = [v_d, v_q, \dot{v}_q, \widehat{\omega}, V_g] \tag{18}$$

with corresponding ground-truth angle $\theta(t)$ obtained from the grid emulator.

4.4.2. Training Setup

- The data is partitioned into training (70%), validation (15%), and testing (15%) subsets.
- Loss function: Mean squared error with regularization (17)
- Optimizer: Adam optimizer
- Epochs: 1000 (as shown in Figure 5)

The trained model is evaluated on unseen disturbance scenarios to ensure generalization capability.

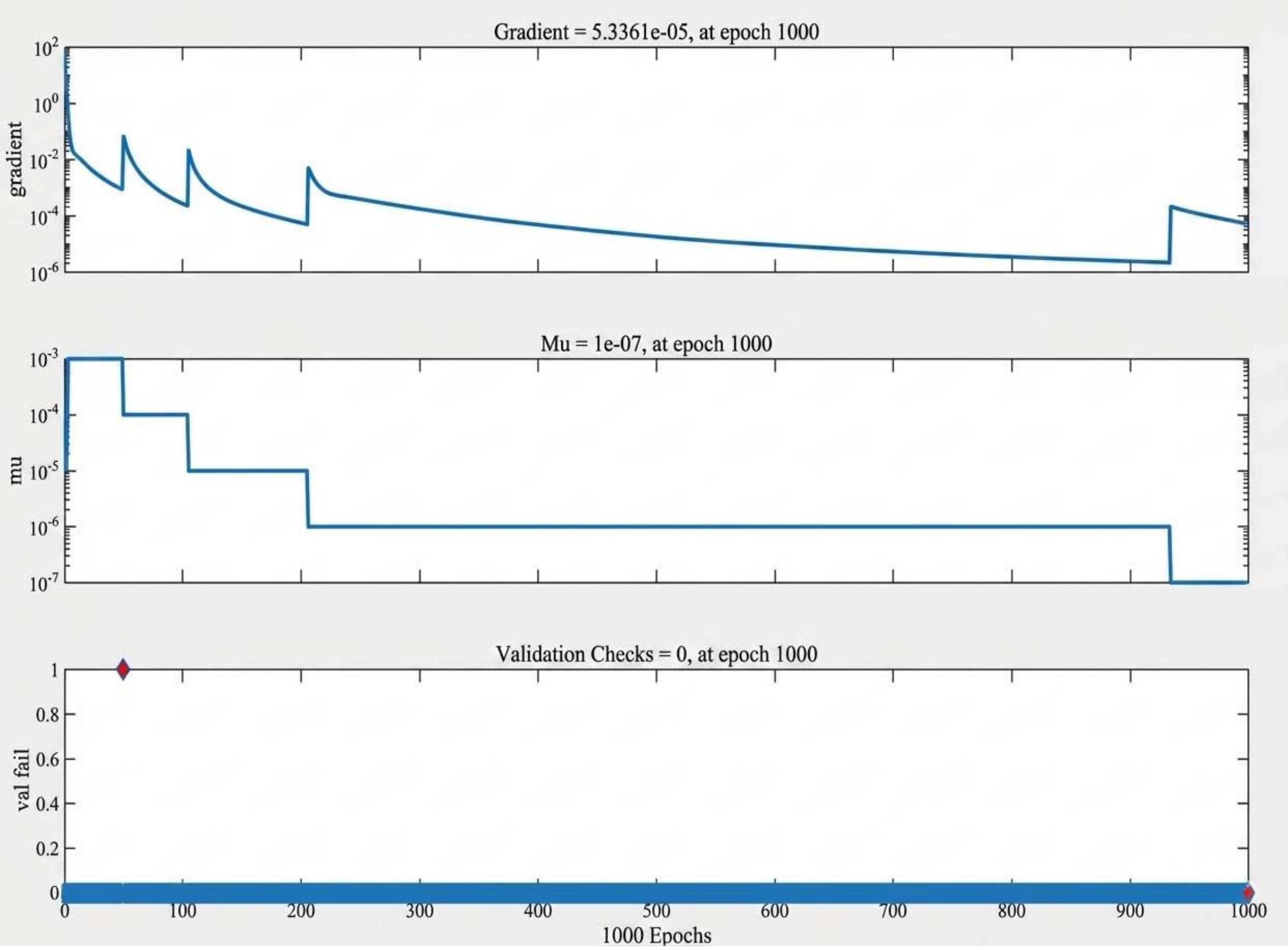

Fig. 4 Training state: gradient, μ, and validation checks (1000 epochs)

4.5. Fault Feature Extraction and Classification Procedure

For event logging and supervisory control under fault conditions, grid and PV disturbances are identified using time–frequency features extracted from the PCC measurements. For a discrete-time signal x[k], the Discrete Wavelet Transform (DWT) provides a multi-resolution decomposition into approximation and detail components across J levels:

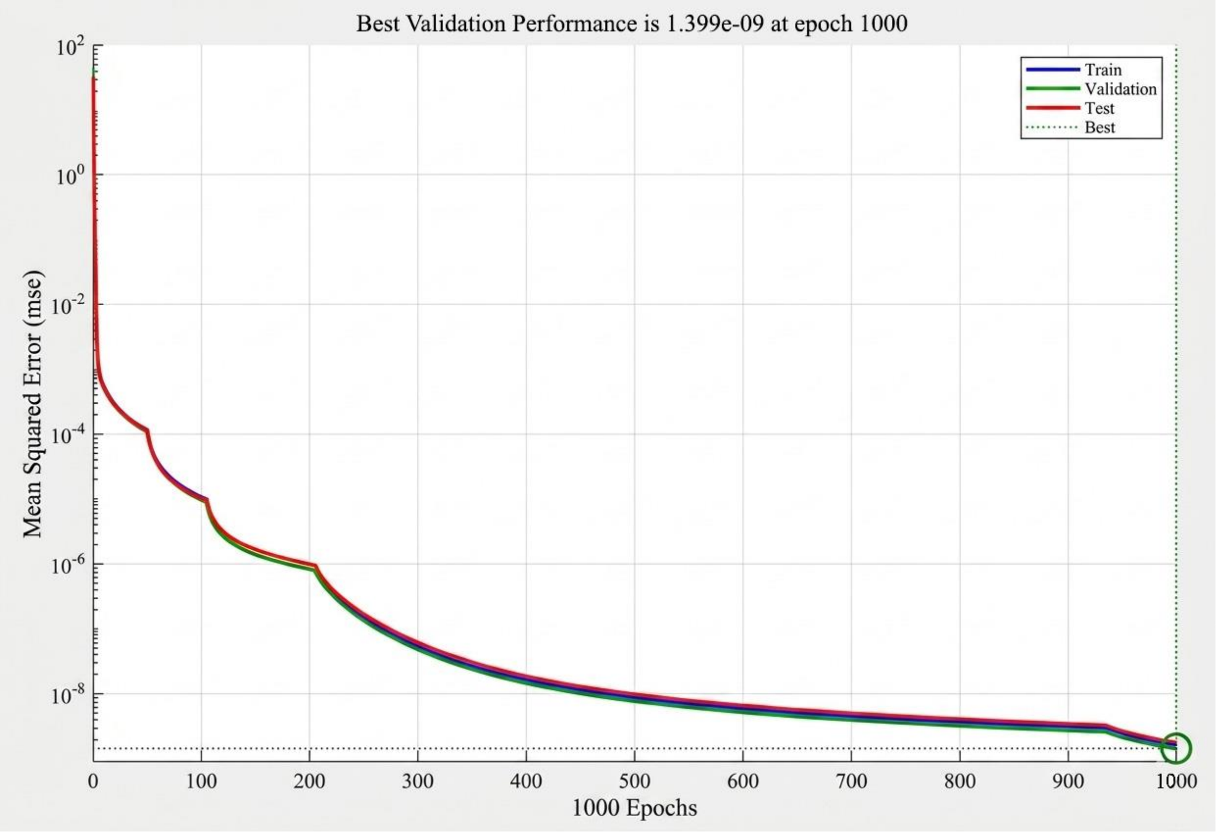

Fig. 5 Training/validation/test MSE vs. epochs (best validation at epoch 1000)

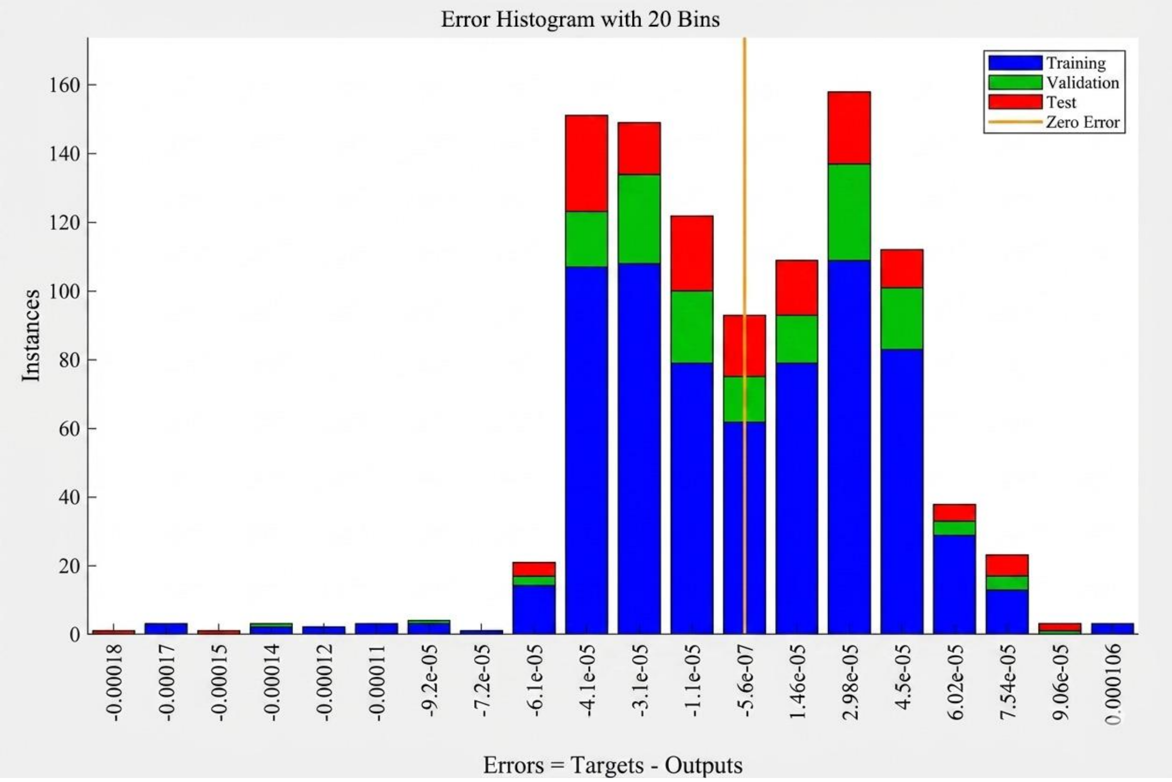

Fig. 6 Histogram of prediction errors (20 bins) across training, validation, and test sets

$$x[k] = \sum_n a_{J.n}\, \phi_{J.n}[k] + \sum_{j=1}^{J} \sum_n d_{J.n}\, \psi_{j,n}[k] \quad (19)$$

where $x[k]$ represents the sampled signal, k is the discrete time index, and J denotes the number of decomposition levels. The coefficients $a_{J.n}$ correspond to the approximation (low-frequency) components at level J, while $d_{J.n}$ represent the detail (high-frequency) components at level j. The functions $\phi_{J.n}[k]$ and $\psi_{j,n}[k]$ denote the scaling and wavelet basis functions, respectively, and n is the translation index.

Feature extraction is performed by computing the energy of each detail sub-band:

$$E_j = \sum_n \left| d_{J.n} \right|^2, \quad f = [E_1, \ldots . E_J, RMS(x), THD(x)]^T \quad (20)$$

where E_j denotes the energy of the jth sub-band, and f is the resulting feature vector. Additional features include the root-mean-square value $RMS(x)$ and total harmonic distortion $THD(x)$ computed over the selected analysis window. The feature vector is normalized prior to classification.

A Multilayer Perceptron (MLP) is employed to estimate the posterior probabilities of disturbance classes:

$$\mathrm{p} = softmax(W_2 \sigma\, W_1 f + b_1) + b_2 \quad (21)$$

where $\mathrm{p} \in \mathbb{R}^C$ represents the probability distribution over C classes. The matrices W_1 and W_2 denote the network weights, b_1 and b_2 are bias vectors, and σ(·) is a nonlinear activation function.

The network parameters are optimized by minimizing the cross-entropy loss function:

$$\mathcal{L}_{CE} = -\frac{1}{N} \sum_{k=1}^{N} \sum_{c=1}^{C} y_{k,c} \log p_{k,c} \quad (22)$$

where $\mathcal{L}_{CE}$ is the loss function, N is the number of training samples, and C is the number of classes. The variable $y_{k,c}$ denotes the one-hot encoded label for sample k, and $p_{k,c}$ is the predicted probability of class c for that sample.

$$i_q^*(t) = sat\left(k_q \frac{V_{nom} - V_g}{V_{nom-}} - I_{max}, I_{max}\right), \; i_q^*(t) = sat\left(\frac{2}{3} \frac{P^*}{\max(V_g, \mathcal{E})}, -\sqrt{I_{max}^2 - {i_q^*}^2}\right) \quad (23)$$

$$\chi(t) = \left(V_{dc}(t) > V_{dc,max}\right) \vee (\|i(t)\| > I_{max}) \vee \left(V_g(t) < V_{min}\right) \quad (24)$$

4.6. Intelligent FRT Policy

During voltage sag conditions, the supervisory FRT mechanism dynamically generates the current references. (i_d^*, i_q^*) to maintain compliance with the inverter current limit I_{max}, and the accumulated violation time

$$\tau(t) = \int_{t_0}^{t} \chi(\xi) \mathrm{d}(\xi) \quad (25)$$

The trip command is issued only when the violation persists beyond the grace period:

$$Trip(t) = \left(\tau(t) \geq T_{grace}\right) \quad (26)$$

where χ(t) is a Boolean indicator that equals 1 when any protection limit is violated and 0 otherwise, $V_{dc,max}$ is the DC-link overvoltage threshold, i(t) is the inverter output current vector in the chosen reference frame, ‖and i(t)‖ is its magnitude, V_{min} is the minimum allowable grid-voltage magnitude for ride-through, $\tau(t)$ is the accumulated time for which violations have been present since t_0, t_0 is the start time of the monitoring interval, ξ is the integration variable,

T_{grace} is the grace period, I(·) is the indicator function that returns 1 if its argument is true and 0 otherwise, and $Trip(t)$ is the trip command.

4.7. Experimental Setup and Test Protocol

The experimental platform comprises a programmable PV source, a grid-connected inverter, an L-type filter, and a programmable grid emulator at the PCC (Figure 3). The test protocol is designed to separately validate the digital twin, synchronization performance, and FRT behavior:

1. Twin Validation: Apply sags according to (11) and record V_{dc} and dq currents to compare measured trajectories against digital-twin predictions using (1)-(7).

2. Synchronization Tests: Superimpose waveform distortion during sags and compare the baseline SRF-PLL (14)-(15) against the augmented PLL (16)-(17) using phase-tracking error and current-quality indices.

3. FRT Tests: Apply deep sags and evaluate current limiting and DC-link containment under the reference law (23) and the trip arbitration in (26).

where PCC indicates the point of common coupling between the inverter and the grid emulator. The L-type filter represents the series interface inductance at the inverter output. The dq currents correspond to the inverter output current components in the SRF.

The phase-tracking error reflects the deviation between the estimated and actual grid angles, whereas current-quality indices refer to standard power quality metrics, including harmonic distortion and unbalance, used for performance comparison.

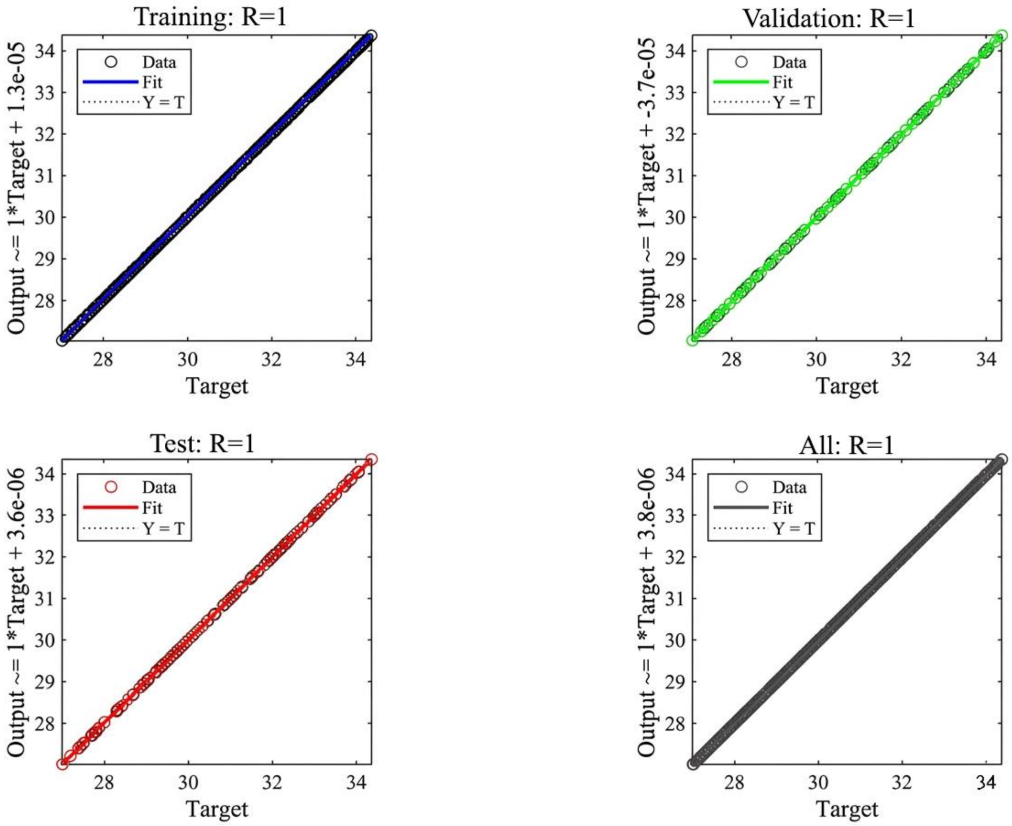

Fig. 7 Regression plots for train/validation/test showing perfect fit (R = 1)

5. Experimental Validation and Results

The Digital Twin (DT), synchronization, and FRT functions were implemented to enable disturbance replay and closed-loop evaluation using MATLAB / Simulink version R2024b. The experimental measurements were carried out by connecting the programmable PV source and grid emulator at the PCC, with supervisory control and data acquisition in NI LabVIEW (2025 Q3). A computer with an Intel Core i5 processor and 16GB RAM performed all the simulations and post-processing operations. Unless stated otherwise, all plots are interpreted over three distinct intervals: (i) pre-disturbance steady state, (ii) the disturbance window, and (iii) post-disturbance recovery.

All figures are presented with clearly marked disturbance intervals, including pre-disturbance, disturbance, and post-disturbance regions. Key variables such as DC-link voltage, active/reactive power, and phase angle are plotted simultaneously to facilitate direct comparison between methods.

5.1. Performance Metrics

To quantitatively evaluate the proposed method, the following performance metrics are used:

- Phase Tracking Error (PTE)

$$PTE = \sqrt{\frac{1}{N}\sum_{k=1}^{N}\left(\theta[k] - \hat{\theta}[k]\right)^2} \quad (27)$$

- Total Harmonic Distortion (THD): Measured from inverter output current using the standard FFT-based definition.
- DC-Link Voltage Deviation (ΔV_{dc}):

$$\Delta V_{dc} = max\left|V_{dc}(t) - V_{dc,ref}\right| \quad (28)$$

- Settling Time (T_s): Time required for system variables to return within ±2% of steady-state after disturbance.

These metrics allow objective comparison between conventional and proposed control strategies.

5.2. Digital Twin Validation

Case A: Voltage Drop Event- Figure 8 illustrates the inverter response under a grid-voltage sag condition. Prior to the disturbance, the PCC voltage remains close to the nominal value. V_{nom}, the inverter supplies the scheduled active power, and the DC-link voltage is maintained near its reference level. At the instant of fault initiation (t_f)The PCC voltage drops, forcing the inverter to operate within the current-limited region. Consequently, the inverter is unable to deliver the pre-disturbance active power. The resulting imbalance between input and output power is reflected in the DC-link dynamics described by (7). During the sag interval, the term $\frac{3}{2}\left(\frac{v_d i_d + v_q i_q}{V_{dc}}\right)$ decreases, leading to an accumulation of excess energy and a rise in V_{dc}.

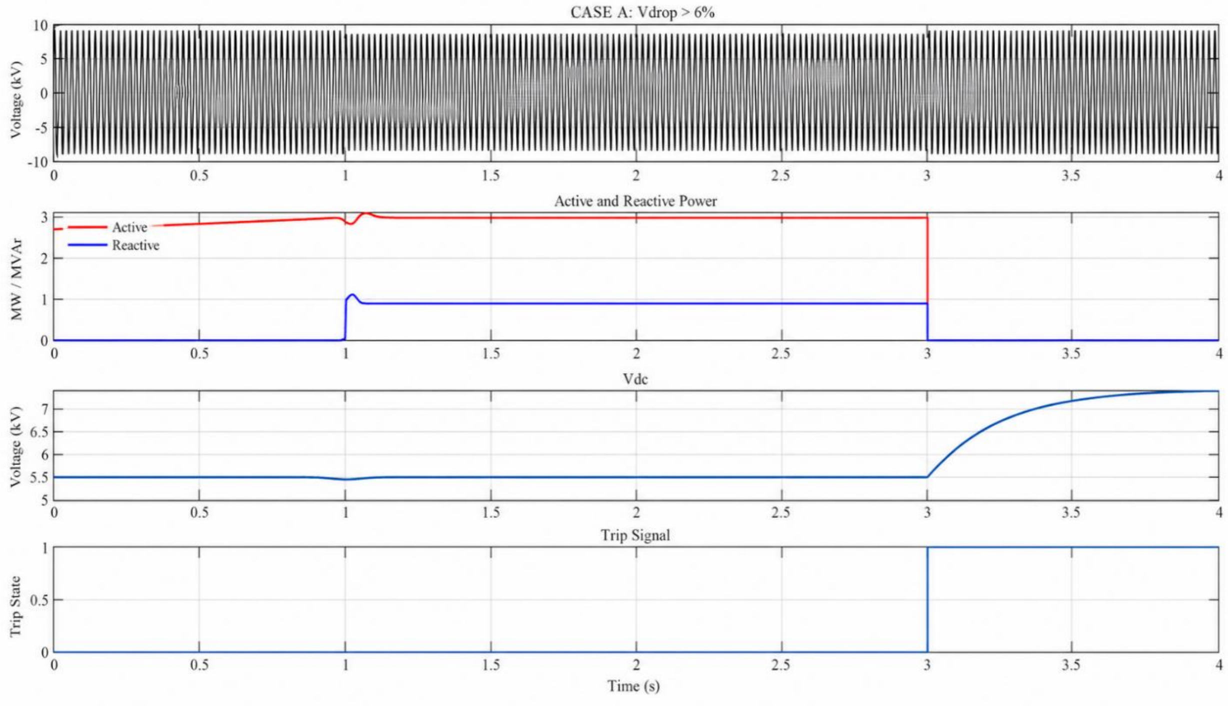

Fig. 8 Case A: Grid voltage, active and reactive power, DC-link voltage, and trip signal during a voltage drop event

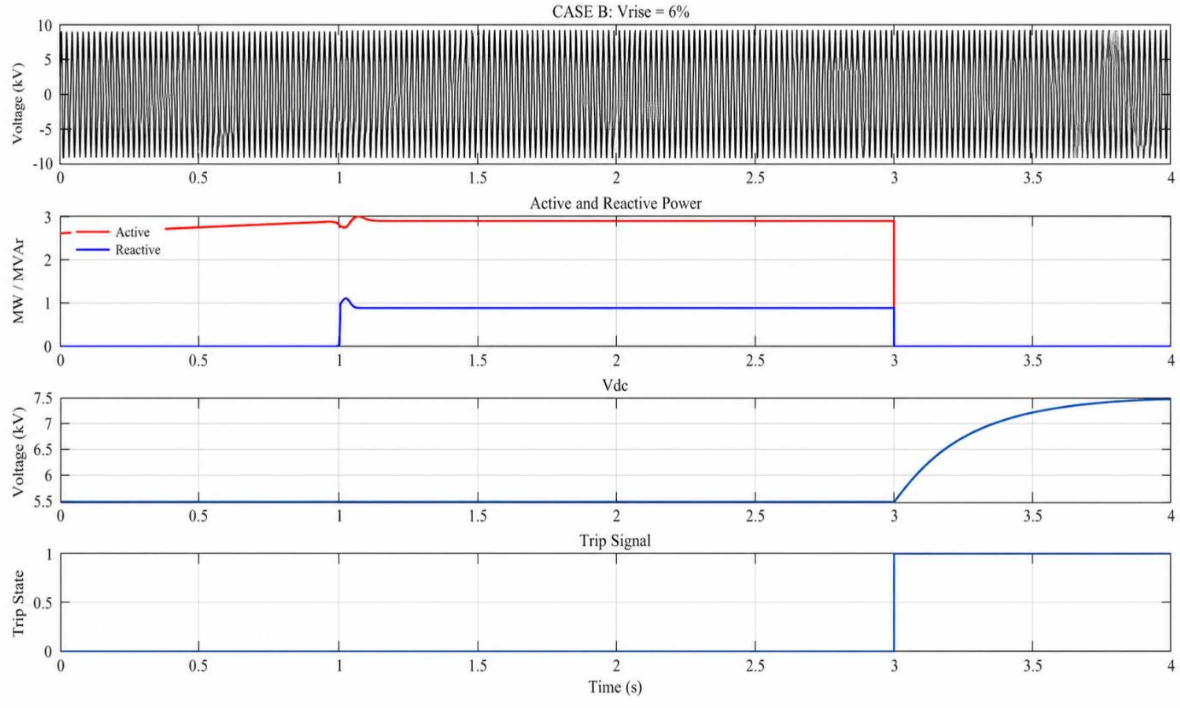

Fig. 9 Case B: Response during a 6% voltage rise event

Case B: Voltage Rise Event- Figure 9 shows the inverter reaction to a 6% voltage rise event. In this case, the PCC voltage exceeds the nominal value, thus changing the inverter operating point and the corresponding current demand for power transfer and voltage support.

The plots confirm the digital twin validation process for overvoltage conditions, where the DT correctly captures the expected direction of the transient and the typical time scale of the recovery process after the voltage restoration.

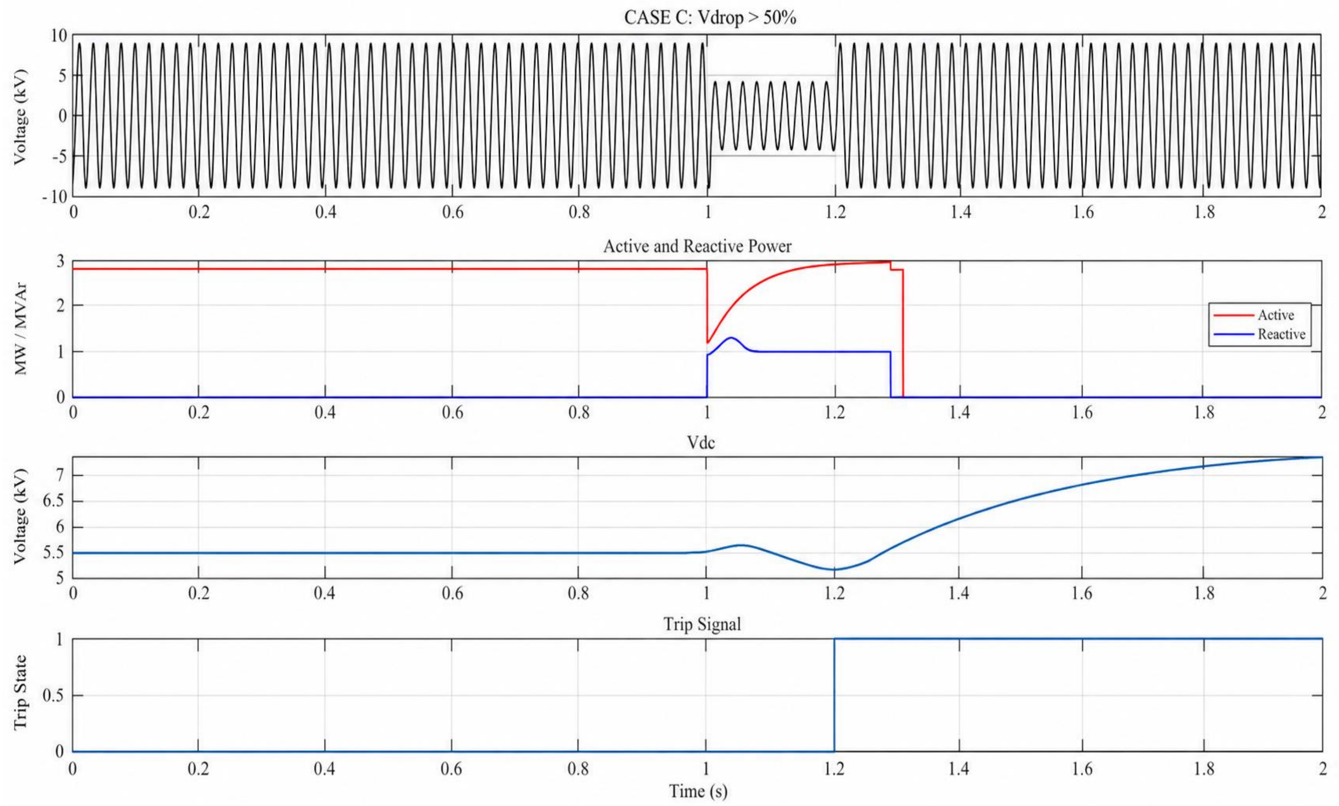

Fig. 10 Case C: Response during a deep voltage drop exceeding 50%

The power plot is considered in Figure 9; the sign and magnitude of the reactive power plot confirm the voltage support strategy adopted during the voltage swell (e.g., reactive power absorption to enable voltage reduction).

5.3. Synchronization Performance Under Sag and Distortion

Figure 10 shows a comparison of phase angle tracking performance between the original SRF-PLL and the proposed augmented PLL during a deep voltage sag of over 50% amplitude. In the original SRF-PLL, the phase error signal is obtained from the q-axis voltage, as defined in Equation (14). During a deep sag and distorted voltage waveform, the q-axis voltage signal v_q contains oscillations and transient errors. These errors are then injected into the PI controller defined in Equation (15), causing ripples and offsets in the estimated angle. $\hat{\theta}$. The figure shows a clear reduction in peak angle error at fault entry for the augmented PLL. It also shows lower oscillatory ripple during the sag interval. This behaviour is similar to that of the correction term in Equation (16), which is trained by the loss function in Equation (17) to reduce the residual tracking error in distorted PCC conditions. The enhancement of angle estimation improves the Park transformation in Equation (9). Concerning angle measurement tracking through a better estimator, the d-q decoupling will be preserved while lowering the cross-coupling of the active current and reactive current channel, while supporting the lower current distortion during the severe grid disturbance.

Case D: Figure 11 shows the inverter response during a grid-frequency increase event. The PLL has a demanding requirement due to frequency excursions, and the state estimate ω ̂ needs to track the transmitted state ω(t) = 2πf(t) well enough to allow carrier distortion. As understood by this illustration, better synchronization holds the current-controller reference frame in line with the grid voltage. Injecting current stays better controlled, and the oscillatory content present in the current waveform improves with this alignment. The figure also indicates an improvement in current- quality metrics, including a reduction in distortion (THD or an equivalent index). Table 5 summarizes the comparative dynamic response of Cases A-D in terms of active/reactive power behavior, DC-link voltage trend, and trip action under different grid disturbances.

5.4. Ablation Study

To evaluate the contribution of each component in the proposed framework, an ablation study is conducted by selectively removing key elements and comparing performance.

Case 1: Baseline SRF-PLL (No AI, No DT) Standard PLL without learning or digital twin support.

Case 2: SRF-PLL + DT (No AI) Digital twin used for parameter tuning, but no AI correction.

Case 3: AI-PLL (No DT) AI-assisted PLL without digital twin calibration.

Case 4: Proposed Method (DT + AI-PLL + FRT)

5.4.1. Performance Metrics

- Phase tracking error (rad)
- Total Harmonic Distortion (THD)
- Peak DC-link voltage deviation

The results show that the combination of digital twin and AI-assisted control provides the best performance, confirming the effectiveness of the integrated framework.

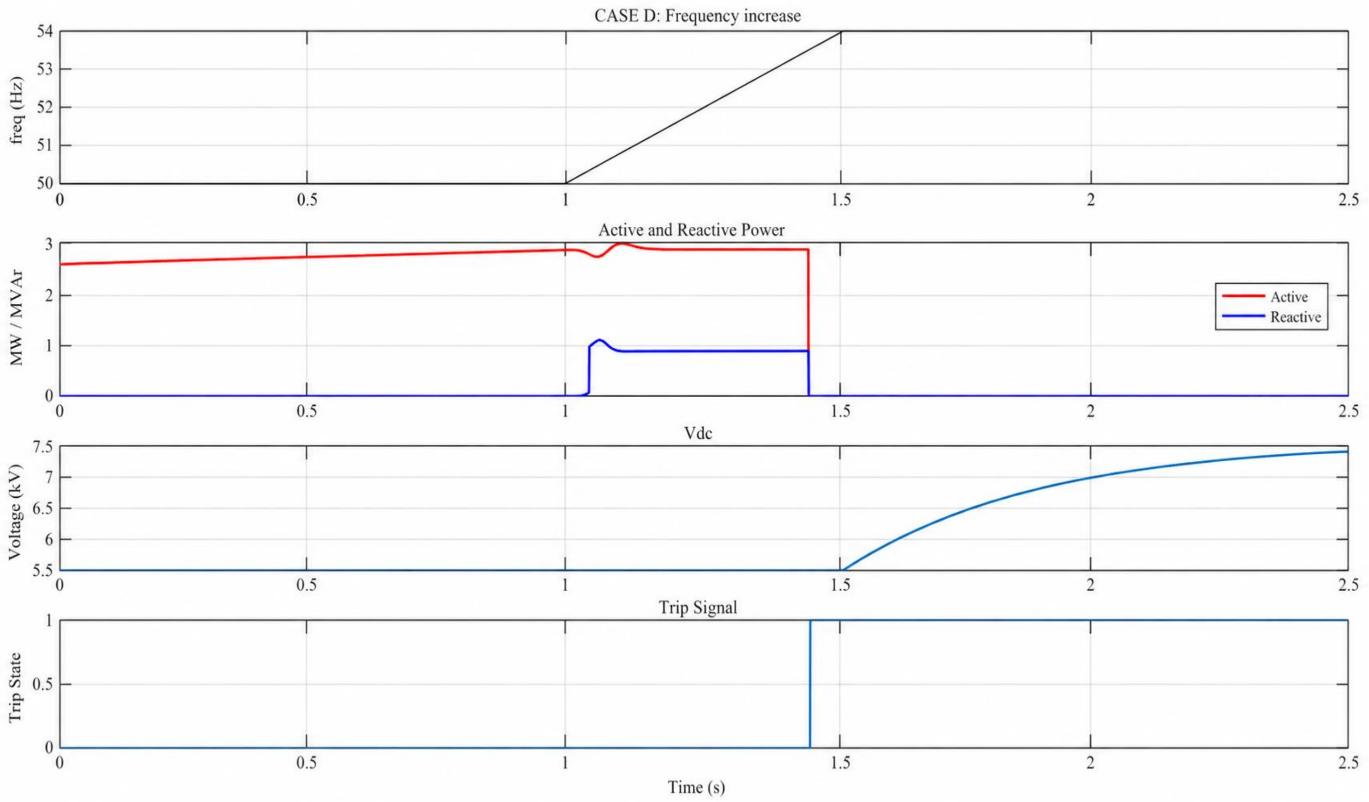

Fig. 11 Case D: Response during a frequency increase event

Table 5. Short comparison of Cases A-D (approximate from plots)

Case	Disturbance	Findings	Comparison
A	Vdrop > 6%	*P* shows a small dip, *Q* rises to ~0.9 MVAr, V_{dc} stays near nominal, and trips at ~3 s.	Stable mild-sag Response with low stress.
B	Vrise = 6%	*P* remains near nominal, *Q* rises with a small overshoot, V_{dc} remains stable, and the trip lasts ~3 s.	Similar to Case A, strong DC-link regulation.
C	Vdrop > 50%	*P* drops sharply, *Q* has the highest overshoot, V_{dc} shows a bump/dip, and trips at ~1.2 s.	Most severe case; fastest protection action.
D	Frequency increase	*P* remains near nominal, *Q* rises, V_{dc} stays stable during ramp, trip at ~1.45 s.	Sync/protection-driven event; lower stress than Case C.

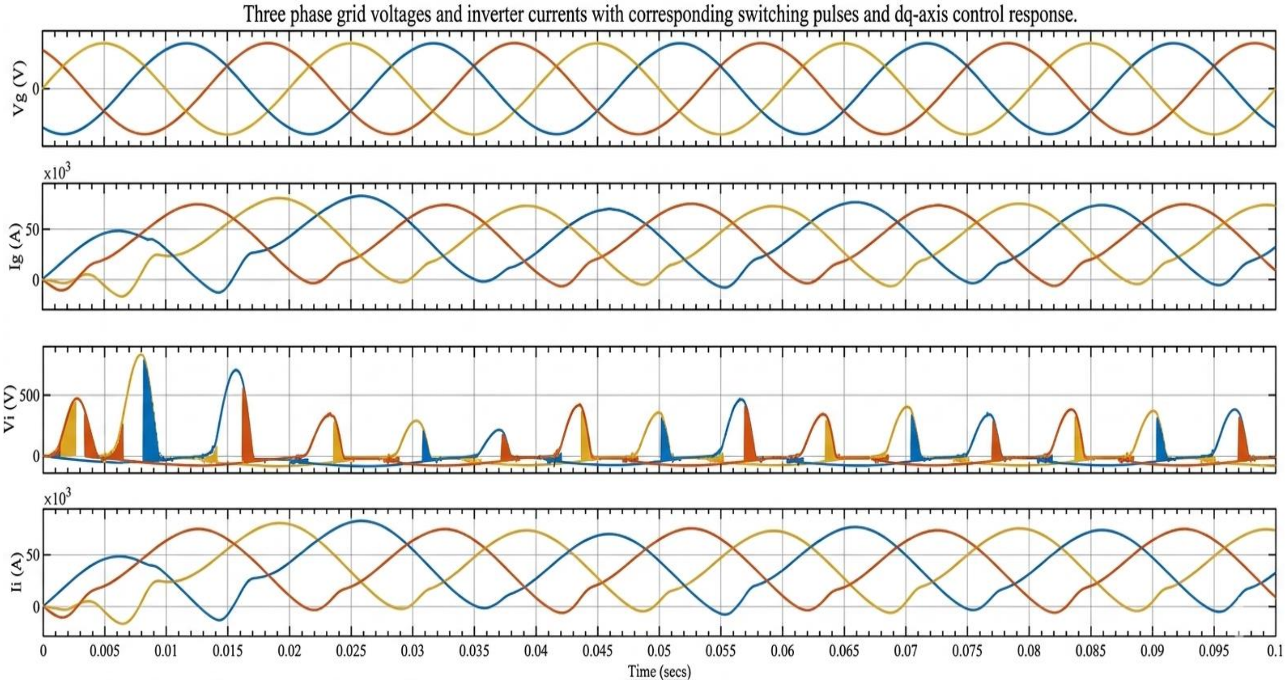

Fig. 12 **Three-phase grid voltages and inverter currents with corresponding switching pulses and *dq*-axis control response**

5.5. FRT Behavior

Deep-Sag Ride-Through- Figure 12 presents the complete ride-through response for a deep sag, including three-phase grid voltages, inverter output currents, switching pulses, and the d-q control signals. At sag entry, the supervisory FRT layer updates the current references using Equation (23).

The controller increases the reactive current reference to support grid voltage and reduces the active current reference to keep the total current within the limit Imax. This current reallocation also limits DC-link stress through the power-balance dynamics of Equation (7). The waveforms in Figure 12 remain limited during the complete sagging phase. In accordance with Equation (23), the present observation affirms the proper functioning of the saturation and circular current-limiting functions.

The figure also indicates a greater contribution of reactive current during the fault, which is in line with grid-support operation under under-voltage conditions. The d-q control signals display the anticipated transition, with the reactive channel increasing during a sag and the active channel reducing. Switching pulses continuously exist; stable operation as the converter does not lose gating during disturbance. The standard SRF-PLL and FRT methods are used to benchmark the method proposed. The proposed framework exhibits obvious enhancements in synchronization accuracy, power quality, and DC link stability when compared to these baseline methods under identical disturbance conditions.

6. Reproducibility and Data Availability

To ensure reproducibility, the following implementation details are provided:

- Simulation platform: MATLAB/Simulink R2024b
- Hardware interface: NI LabVIEW with programmable PV and grid emulator
- Neural network: feedforward MLP with one hidden layer
- Training data: generated using a digital twin and validated using experimental measurements

The dataset generation procedure, model architecture, and training configuration are fully described in Section 4. Additional implementation details, including model parameters and simulation scripts, can be made available upon request. Future work will include releasing a standardized dataset and code repository to enhance reproducibility further.

Table 6. Ablation study results

Method	Phase Error	THD (%)	V_{dc} Deviation
Baseline PLL	High	6.5	High
PLL + DT	Medium	5.2	Medium
AI-PLL only	Medium-Low	4.3	Medium
Proposed Method	Low	3.1	Low

7. Conclusion

The control scheme based on the digital twin for the grid-connected PV inverter in low-voltage grids, along with voltage sag, voltage swell, and frequency change, is presented in this paper. The digital twin model correctly represents the key dynamics between the PV source, the DC link, and the converter. The inverter's transient response is also well modelled and accurate with measurement. This comprises the dynamic behavior of active and reactive power, the DC-link voltage dynamic behavior, and the triggers for the tripping actions. The case studies presented above illustrate the technical behavior in a clear and comprehensible manner. In Case A and Case B, where a small sag or swell occurs, the inverter retains the active power level close to nominal after a transient period.

The reactive power gets increased to 0.9 MVAr with a slight overshoot, and the dc-link voltage remains near its nominal value under normal conditions. In Case C, there is a deep sag of more than 50% voltage reduction, whereas the active power has a sharp drop at the entry of the fault. The reactive power has the largest overshoot, ranging from 1.35 to 1.4 MVAr, and the trip signal is activated first among the cases, showing proper current limiting and fast protection activation under heavy stress. In Case D, with a frequency increase, the power loop remains stable, and the main impact is on the synchronization and trip timing. The control scheme shows excellent consistency between the digital twin and the actual inverter behavior, with stable control in non-ideal grid conditions and proper fault-ride-through and protection activation.

Despite its advantages, the proposed framework has certain the proposed framework has certain limitations:

- Model Accuracy: The effectiveness of the digital twin depends on accurate parameter calibration. Model mismatch may reduce prediction accuracy under changing operating conditions.
- Training Data Dependency: The performance of the AI-assisted PLL depends on the diversity and quality of training data. Extreme or unseen grid disturbances may affect performance.
- Communication and Latency: If implemented in a distributed or edge-computing environment, communication delays may impact real-time decision-making.
- Implementation Cost: Additional computational resources and system integration effort may increase the initial deployment cost compared to conventional control strategies.

Conflicts of Interest

It is hereby declared by the authors that there exists no competing financial concern or personal association that may be construed as having influenced the contents of the present manuscript.

Funding Statement

No external funding has been availed by the authors for carrying out this study or for the preparation and submission of this article.

References

[1] IEEE Standards Coordinating Committee 21, *IEEE Standard for Interconnection and Interoperability of Distributed Energy Resources with Associated Electric Power Systems Interfaces*, IEEE Std 1547-2018, pp. 1-138, 2018. [CrossRef] [Google Scholar] [Publisher Link]

[2] Asma Triki-Lahiani, Afef Bennani-Ben Abdelghani, and Ilhem Slama-Belkhodja, "Fault Detection and Monitoring Systems for Photovoltaic Installations: A Review," *Renewable and Sustainable Energy Reviews*, vol. 82, pp. 2680-2692, 2018. [CrossRef] [Google Scholar] [Publisher Link]

[3] Weidong Xiao, *Photovoltaic Power System: Modeling, Design, and Control*, Wiley, 2017. [Google Scholar] [Publisher Link]

[4] Albert Yaw Appiah et al., "Review and Performance Evaluation of Photovoltaic Array Fault Detection and Diagnosis Techniques," *International Journal of Photoenergy*, vol. 2019, no. 1, pp. 1-19, 2019. [CrossRef] [Google Scholar] [Publisher Link]

[5] Mohammadreza Aghaei et al., "Fault Inspection by Aerial Infrared Thermography in a PV Plant after a Meteorological Tsunami," *Anais Congresso Brasileiro de Energia Solar (CBENS)*, pp. 1-9, 2018. [CrossRef] [Google Scholar] [Publisher Link]

[6] L. Schirone et al., "Fault Finding in a 1 MW Photovoltaic Plant by Reflectometry," *Proceedings of the IEEE 1st World Conference on Photovoltaic Energy Conversion (WCPEC)*, Waikoloa, HI, USA, vol. 1, pp. 846-849, 1994. [CrossRef] [Google Scholar] [Publisher Link]

[7] Mahmoud Dhimish, and Violeta Holmes, "Fault Detection Algorithm for Grid-Connected Photovoltaic Plants," *Solar Energy*, vol. 137, pp. 236-245, 2016. [CrossRef] [Google Scholar] [Publisher Link]

[8] Elyes Garoudja et al., "Statistical Fault Detection in Photovoltaic Systems," *Solar Energy*, vol. 150, pp. 485-499, 2017. [CrossRef] [Google Scholar] [Publisher Link]

[9] Chenxi Li et al., "A Fast MPPT-Based Anomaly Detection and Accurate Fault Diagnosis Technique for PV Arrays," *Energy Conversion and Management*, vol. 234, 2021. [CrossRef] [Google Scholar] [Publisher Link]

[10] Jianing Wu, and Shaoze Yan, and Liyang Xie "Reliability Analysis Method of a Solar Array by Using Fault Tree Analysis and Fuzzy Reasoning Petri Net," *Acta Astronautica*, vol. 69, no. 11-12, pp. 960-968, 2011. [CrossRef] [Google Scholar] [Publisher Link]

[11] Renewables 2024, International Energy Agency, 2024. [Online]. Available: https://www.iea.org/reports/renewables-2024

[12] Aishwarya S. Mundada, Emily W. Prehoda, and Joshua M. Pearce, “U.S. Market for Solar Photovoltaic Plug-and-Play Systems,” *Renewable Energy*, vol. 103, pp. 255-264, 2017. [CrossRef] [Google Scholar] [Publisher Link]

[13] National Renewable Energy Laboratory, Best Research-Cell Efficiencies, NREL, [Online]. Available: https://www.nlr.gov/pv/cell-efficiency

[14] A. Chouder, and S. Silvestre, “Analysis Model of Mismatch Power Losses in PV Systems,” *Journal of Solar Energy Engineering*, vol. 131, no. 2, 2009. [CrossRef] [Google Scholar] [Publisher Link]

[15] Silvano Vergura et al., “Inferential Statistics for Monitoring and Fault Forecasting of PV Plants,” *2008 IEEE International Symposium on Industrial Electronics*, Cambridge, UK, pp. 2414-2419, 2008. [CrossRef] [Google Scholar] [Publisher Link]

[16] Ye Zhao et al., “Graph-Based Semi-Supervised Learning for Fault Detection and Classification in Solar Photovoltaic Arrays,” *IEEE Transactions on Power Electronics*, vol. 30, no. 5, pp. 2848-2858, 2015. [CrossRef] [Google Scholar] [Publisher Link]

[17] M. Sabbaghpur Arani, and M. A. Hejazi, “The Comprehensive Study of Electrical Faults in PV Arrays,” *Journal of Electrical and Computer Engineering*, vol. 2016, no. 1, pp. 1-10, 2016. [CrossRef] [Google Scholar] [Publisher Link]

[18] Wenjie Ma, Sen Ouyang, and Weidong Xu, “Improved Frequency Locked Loop Based Synchronization Method for Three Phase Grid-Connected Inverter under Unbalanced and Distorted Grid Conditions,” *Energies*, vol. 12, no. 6, pp. 1-18, 2019. [CrossRef] [Google Scholar] [Publisher Link]

[19] Elutunji Buraimoh, Innocent E. Davidson, and Fernando Martinez-Rodrigo, “Decentralized Fast Delayed Signal Cancelation Secondary Control for Low Voltage Ride-Through Application in Grid Supporting Grid Feeding Microgrid,” *Frontiers in Energy Research*, vol. 9, 2021. [CrossRef] [Google Scholar] [Publisher Link]

[20] Mehrdad Tarafdar Hagh, and Tohid Khalili, “A Review of Fault Ride through of PV and Wind Renewable Energies in Grid Codes,” *International Journal of Energy Research*, vol. 43, no. 4, pp. 1342-1356, 2018. [CrossRef] [Google Scholar] [Publisher Link]

[21] Nishij G. Kulkarni, and Vasudeo B. Virulkar, “Enhancing the Power Quality of Grid Connected Photovoltaic System during Fault Ride Through: A Comprehensive Overview,” *Journal of the Institution of Engineers (India): Series B*, vol. 104, no. 3, pp. 821-836, 2023. [CrossRef] [Google Scholar] [Publisher Link]

[22] Dorotea Dimitrova Angelova et al., “A Review on Digital Twins and Its Application in the Modelling of Photovoltaic Installations,” *Energies*, vol. 17, no. 5, pp. 1-29, 2024. [CrossRef] [Google Scholar] [Publisher Link]

[23] Wulfran Fendzi Mbasso et al., “Digital Twins in Renewable Energy Systems: A Comprehensive Review of Concepts, Applications, and Future Directions,” *Energy Strategy Reviews*, vol. 61, pp. 1-21, 2025. [CrossRef] [Google Scholar] [Publisher Link]